# DEVELOPMENT OF AN ATTITUDE DETERMINATION AND CONTROL STRATEGY FOR THE ST3LLARSAT1 CUBESAT MISSION

**Ghasem Sharifi**[(1)], **Andrés Rabuñal**[(1)], **Diego Navarro-Tapia**[(1)], **Andrés Marcos**[(1)]

[(1)] *Aerospace Engineering Department, Universidad Carlos III de Madrid (UC3M), Madrid, Spain*

## ABSTRACT

This paper presents the development of the attitude determination and control subsystem (ADCS) for ST3LLARsat1 "BOIRA", a 2U student CubeSat mission aimed at educational and scientific objectives, specifically, measuring atmospheric water vapor. The mission comprises two main ADCS operational modes: detumbling and attitude pointing. Currently, three detumbling control solutions have been defined, and are presented and compared here in terms of key factors such as detumbling time and power consumption. For the attitude pointing mode, mainly for nadir, a hybrid approach combining the Triad method and an extended Kalman filter is employed for determination, and a sliding mode approach for the attitude pointing, which is actuated using only magnetic-torquers. Model in the loop simulation results conducted using MATLAB/Simulink indicate that the designed B-dot controller fulfills our mission detumbling requirements, and that the attitude pointing controller can provide a nadir attitude knowledge error and an attitude pointing error of respectively $\leq 3$ and 5 degrees. A Monte Carlo campaign, under various disturbances and uncertain parameters, was also conducted to validate the performance of the developed algorithms.

## 1 INTRODUCTION

The Attitude Determination and Control Subsystem (ADCS) is one of the challenging and crucial subsystems of a satellite, responsible for providing attitude and stability required for the mission. The attitude control solution implemented for ST3LLARsat1 relies on a fully magnetic actuation system, employing a combination of three orthogonal magnetorquers. The use of magnetic actuators offers several advantages, including low power consumption, compact volume, and minimal mass [1]. However, the spacecraft's control is underactuated, meaning that it lacks sufficient control inputs to address all degrees of freedom simultaneously. Specifically, the magnetic actuators can only supply control torque perpendicular to the geomagnetic field vector. This limitation restricts the spacecraft's ability to maneuver in certain directions [2, 3]. A significant body of research has focused on the analysis and design of magnetic control laws in the linear regime [4, 5, 6], specifically addressing control laws for the nominal operation of satellites near their equilibrium attitude. In [7], feedback laws achieving local exponential stability, even in the presence of substantial uncertainties in the spacecraft's inertia matrix, were proposed. The Sliding Mode Control (SMC) for attitude stabilization of satellites has been proposed as a solution, even in cases where pure magnetic actuators are employed [8, 9, 10].

Satellite attitude determination is another critical aspect of ADCS subsystem design, as it provides essential attitude estimation for effective control. However, this task becomes particularly challenging when using Commercial Off-The-Shelf (COTS) equipment. To address this challenge, a hybrid approach that combines the Triad method [11, 12] with the Extended Kalman Filter (EKF) algorithm is proposed for ST3LLARsat1. This integration leverages the simplicity of the Triad

method, which uses vector observations, while also harnessing the accuracy and adaptability of the EKF approach. The Kalman filter [13] has emerged as the predominant framework for developing orientation filter algorithms [1, 14], as well as for powering commercial inertial orientation sensors. Notably, companies such as Xsens [15], Micro-strain [16], VectorNav [17], Intersense [18] have built their systems around the principles of the Kalman filter. This widespread reliance on Kalman-based solutions underscores their reputation for providing highly accurate and effective orientation estimation.

The layout of the article is as follows. Section 2 describes the ST3LLARsat1 mission. Section 3 presents the ADCS scheme covering the equipment and connection of algorithms. Subsequently, the methods for attitude determination and control are presented in Section 4, whereas Section 5 discusses the results of ADCS simulations. Finally, conclusions are given in Section 6.

## 2 DESCRIPTION OF THE MISSION

### 2.1 Mission description and requirements

ST3LLARsat1 "BOIRA" is the first student CubeSat established at the Universidad Carlos III de Madrid (UC3M). The student CubeSat program started in September 2022 and was selected by the European Space Agency (ESA) in December 2022 for participation in its pilot Fly Your Satellite! (FYS!) Design Booster program. This ESA initiative aims to assist European university teams to consolidate their CubeSat designs. This program lasts 1.5 years and will finish in May 2024.

The primary objective of ST3LLARsat1 is to design, integrate, validate, launch, and operate a 2U CubeSat, primarily focused on educational purposes, with secondary objectives related to technology demonstration and scientific exploration. The educational aspect involves providing students with practical involvement in a real space project through a blend of theoretical learning and hands-on application. The technological goals include demonstrating two in-house developed innovations: a compact, dual-circular, non-deployable antenna; and an on-board computer architecture capable of including advanced ADCS algorithms coded in-house. Additionally, from a scientific standpoint, the mission aims to demonstrate that atmospheric water vapor measurements can be taken in such a small spacecraft and using a COTS spectrometer.

The main technical specifications for the mission as well as the ADCS subsystem requirements are detailed in Table 1. The nominal orbit is a circular, Low Earth Orbit (LEO) with the orbital parameters given in the table. And the flowed-down ADCS requirements shown in the table were obtained based on mission analysis and the payload characteristics for a range of orbits. Further information on the mass properties of the components and CubeSat are found in subsequent sections (see for example, Table 2 and Table 3).

Table 1: ST3LLARsat1 technical specifications and ADCS requirements.

| Parameter | Symbol | Value | Parameter | Symbol | Value |
|---|---|---|---|---|---|
| Size | $S_c$ | 2U | Orbital Altitude | $Alt$ | $425\,\mathrm{km}$ |
| Mass | $M$ | $1.65\,\mathrm{kg}$ | Orbital inclination | $i$ | $97.12\,\mathrm{deg}$ |
| Power | $P$ | $4.8\,\mathrm{W}$ | Orbital eccentricity | $e$ | 0.0001 |
| TC/TM† Band | $b_T$ | UHF | Attitude Pointing Error | $APE$ | $\leq 10\,\mathrm{deg}$ |
| TC/TM† Frequency | $f_T$ | $435-438\,\mathrm{MHz}$ | Attitude Knowledge Error | $AKE$ | $\leq 5\,\mathrm{deg}$ |

†TC/TM denotes the telecommunication command and telemetry respectively.

### 2.2 Dynamic and Kinematic equations

The dynamics of a satellite within the Earth-Centered Inertial (ECI) frame are governed by Euler's equations of motion, Eq. 1, which describe the changes in angular velocity caused by control $\boldsymbol{T}_c$ and disturbance $\boldsymbol{T}_{dist}$ torques. Changes in angular velocity can be used to determine the variation with time of the quaternions, thereby providing the evolution of the satellite attitude [19, 20], Eq. 2.

$$\boldsymbol{\omega}_{BI} = (I_B)^{-1}[\boldsymbol{T}_c + \boldsymbol{T}_{dist} - \boldsymbol{\omega}_{BI} \times (I_B \boldsymbol{\omega}_{BI})] \tag{1}$$

$$\dot{\boldsymbol{q}} = \frac{1}{2}\Omega(\omega)q = \frac{1}{2}\begin{bmatrix} 0 & \omega_x & -\omega_y & -\omega_z \\ \omega_x & 0 & \omega_z & -\omega_y \\ \omega_y & -\omega_z & 0 & \omega_x \\ \omega_z & \omega_y & -\omega_x & 0 \end{bmatrix}\begin{bmatrix} q_0 \\ q_1 \\ q_2 \\ q_3 \end{bmatrix} \tag{2}$$

Here, $\boldsymbol{\omega}_{BI}$ denotes the angular velocity of the satellite relative to the ECI frame, where the moment of inertia matrix is represented by $I_B$. Additionally, it is noted that the disturbance torque $\boldsymbol{T}_{dist}$ is composed of: the gravity-gradient $\boldsymbol{T}_{gg}$, the residual magnetic $\boldsymbol{T}_{mag}$, the aerodynamic drag $\boldsymbol{T}_a$, and the solar radiation $\boldsymbol{T}_s$ torque components.

As aforementioned, the desired orbit for the ST3LLARsat1 mission is in LEO where atmospheric density, magnetic field, and gravity gradient are quite high. Thus, the disturbance torques have a considerable impact on the satellite dynamics and can be calculated by [1] :

$$\boldsymbol{T}_{\text{gg}} = \frac{3\mu}{\boldsymbol{r}^5}(\boldsymbol{r} \times (I_{\text{B}} \cdot \boldsymbol{r})), \tag{3}$$

$$\boldsymbol{T}_{\text{mag}} = -\boldsymbol{B}_B \times \boldsymbol{m}_{\text{res}}, \tag{4}$$

$$\boldsymbol{T}_a = \sum_{i=1}^{N} \boldsymbol{d_i} \times \boldsymbol{F_a} \tag{5}$$

$$\boldsymbol{T}_s = \sum_{i=1}^{N} \boldsymbol{d_i} \times \boldsymbol{F_s} \tag{6}$$

where $\mu$ is the gravitational parameter, $\boldsymbol{r}$ is the position vector of the center of mass (CoM) of the satellite in the ECI frame, $m_{res}$ is the residual magnetic dipole, $\boldsymbol{B}_B$ is the magnetic field in body-frame coordinates and $\boldsymbol{d}_i$ is the vector from the satellite CoM to the center of pressure of the $i_{th}$ plate. The aerodynamic force ($\boldsymbol{F}_a$) and solar pressure force ($\boldsymbol{F}_s$) are given by [1]:

$$\boldsymbol{F}_a = -\frac{1}{2}\rho C_d \big\|\boldsymbol{v}_{rel\ B}\big\| \boldsymbol{v}_{rel\ B} S_i max(\cos\theta_a, 0) \tag{7}$$

$$\boldsymbol{F}_s = -P_s S_i \big[2(\frac{R^i_{diff}}{3} + R^i_{spec}\cos\theta_s{}^i)\boldsymbol{n}^i_B + (1 - R^i_{spec})\boldsymbol{S_B}\big] max(\cos\theta_s{}^i, 0) \tag{8}$$

where $\rho$ represents the atmospheric density, $C_D$ is a dimensionless drag coefficient, $\mathbf{v}_{\text{rel}\,B}$ is the relative velocity in the body frame, $S$ is the surface area, $\mathbf{n}_B$ is the unit normal vector in the body frame, $P_s$ is the solar radiation pressure, $\mathbf{S_B}$ is the sun vector in the body frame, $R_{\text{diff}}$ is the diffuse reflection coefficient, and $R_{\text{spec}}$ is the specular reflection coefficient. The angles $\theta_a$ and $\theta_s$ represent the inclination of the $i_{\text{th}}$ plate to the relative velocity and solar pressure, provided by $\theta_a = \cos^{-1}\left(\frac{\mathbf{n}^i_B \cdot \mathbf{v}_{\text{rel}\,B}}{\|\mathbf{v}_{\text{rel}}\|}\right)$ and $\theta_s = \mathbf{n}^i_B \cdot \mathbf{s}$, respectively. The max function ensures that only the surfaces facing the flow are taken into account. See Table 3) for the values of the main parameters above.

## 3 ADCS SCHEME

ST3LLARsat1's on-board computing architecture consists of two different microcontrollers: one dedicated to the on-board computer (OBC), serving as the main brain of the satellite for managing and controlling different subsystems; and another microcontroller dedicated to the ADCS subsystem. This approach aims to reduce the computational burden and load on the OBC microcontroller. The two boards are connected to each other using a serial protocol via PC/104 to facilitate the transmission of OBC commands to the ADCS board and the tranmission of satellite attitude, velocity, and position data to the OBC board. Fig. 1 shows the main components related to the ADCS subsystem plus the payload.

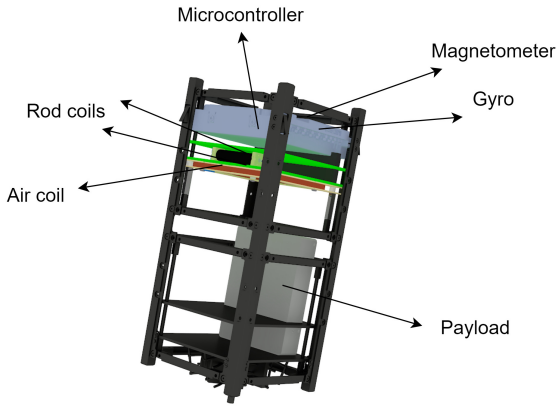


Figure 1: The integration of the ADCS equipment onto the ST3LLARsat1 structure.

The overall ADCS architecture is presented in Fig. 2. The sensors employed are detailed in the left side of the figure. This includes one three-axis gyroscope, one magnetometer, and 16 photodiodes serving as coarse sun sensors. These sensors provide essential measurements for the attitude determination algorithms, which utilize a Triad algorithm to initialize an Extended Kalman filter. Additionally, an orbit propagator is used that utilizes Global Navigation Satellite System (GNSS) data to estimate the CubeSat's orbital position. This propagator is designed to continue propagating the position in case the GNSS equipment is switched off in order to reduce power consumption.

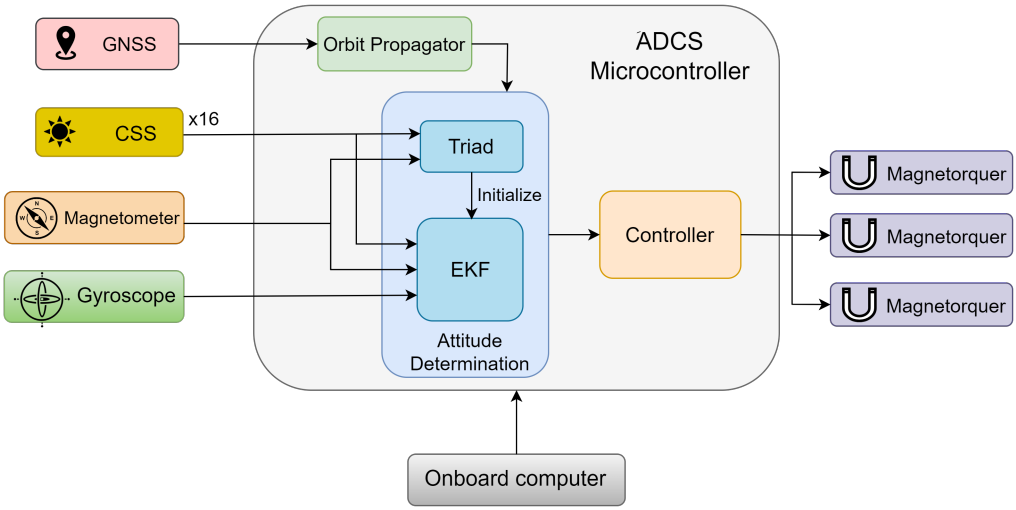


Figure 2: Schematic diagram of the ADCS subsystem

The control function in Fig. 2 includes different control algorithms (see Section 4.2) for the two ADCS operational modes (detumbling and attitude pointing). Finally, the actuation suite is composed of three magnetic torquers (see right side in Fig. 2), comprising two rods and one air coil. They are responsible for generating the required torque on the satellite body to control its orientation.

The list of ADCS components is reported in Table 2. In addition, their mass, power consumption and duty cycle details are also included.

Table 2: ADCS mass and power budget.

| Equipment | Model | Number | Mass ($gr$) | Power ($mW$) | Duty cycle(%) |
|---|---|---|---|---|---|
| Magnetometer | PNI RM3100 | 1 | 0.25 | 2.2 | 20 |
| Photodiode | OSRAM SFH 2401 | 16 | 0.043 | 0.065 | 100 |
| Gyroscope | ADIS16500 | 1 | 1.75 | 200 | 100 |
| GNSS | Orion B16-C1 | 1 | 1.7 | 215 | 100 |
| Magnetorquer rods | CubeSpace CR0002 | 2 | 33 | 327 | 80 |
| Magnetorquer coil | CubeSpace CubeCoil | 1 | 46 | 600 | 80 |
| Microcontroller | Microchip SAMV71Q21 | 1 | 1.365 | 297 | 100 |
| Total | | | 116.985 | 1969.24 | |

## 4 ATTITUDE DETERMINATION AND CONTROL ALGORITHMS

### 4.1 Attitude determination

#### 4.1.1 Tri-Axial Attitude Determination Method (TRIAD)

The TRIAD algorithm is employed to determine the attitude of the CubeSat, using measurements from sun sensors and magnetometer. In our attitude determination strategy, TRIAD's output is used to initialize the Extended Kalman Filter (EKF) algorithms, accelerating its convergence. The output of the algorithm is the rotation matrix from the orbit reference frame to the body reference frame. In the body reference frame, the necessary vectors are determined using available sun sensors and magnetometer. For the orbital frame, the vectors for the magnetic field are computed from the International Geomagnetic Reference Field (IGRF), while the sun vector is obtained from the satellite's location estimated by an orbit propagator or GNSS, with consideration for the current time [11, 12]. The rotation matrix can be calculated by:

$$\boldsymbol{t}_{1B} = \frac{\boldsymbol{S}_B}{\|\boldsymbol{S}_B\|}, \boldsymbol{t}_{2B} = \frac{\boldsymbol{S}_B \times \boldsymbol{B}_B}{\|\boldsymbol{S}_B \times \boldsymbol{B}_B\|}, \boldsymbol{t}_{3B} = \boldsymbol{t}_{1B} \times \boldsymbol{t}_{3B} \tag{9}$$

$$\boldsymbol{t}_{1O} = \frac{\boldsymbol{S}_O}{\|\boldsymbol{S}_O\|}, \boldsymbol{t}_{2O} = \frac{\boldsymbol{S}_O \times \boldsymbol{B}_O}{\|\boldsymbol{S}_O \times \boldsymbol{B}_O\|}, \boldsymbol{t}_{3O} = \boldsymbol{t}_{1O} \times \boldsymbol{t}_{3O} \tag{10}$$

$$R_{O \to B} = [\boldsymbol{t}_{1O}, \boldsymbol{t}_{2O}, \boldsymbol{t}_{3O}] \, [\boldsymbol{t}_{1B}, \boldsymbol{t}_{2B}, \boldsymbol{t}_{3B}]^T \tag{11}$$

where $\boldsymbol{S}_O$ and $\boldsymbol{B}_O$ represent the sun vector and magnetic field in the orbital frame, respectively, while $\boldsymbol{S}_B$ and $\boldsymbol{B}_B$ represent them in the body frame.

#### 4.1.2 Extended Kalman Filter

The Extended Kalman Filter (EKF) is utilized to estimate an orientation represented as a quaternion $q$. Initially, the state is predicted using the measurements from the gyroscopes. Subsequently, this predicted state is refined using measurements from both sun sensors and magnetometer. It is important

to note that gyroscopic data are treated as external inputs to the filter rather than as measurements. Consequently, their measurement noises are incorporated into the filter as process noise rather than as measurement noise [21]. In the designed filter, the quaternion serves as the state vector, while the angular velocity functions as the control vector. The estimation process comprises two primary steps: prediction and correction.

**Prediction**

In the initial step, the quaternion at time $t$ is predicted by integrating the angular rate $\boldsymbol{\omega}_{BI}$ and adding it to the previously computed quaternion $\boldsymbol{q}_{t-1}$. This process can be summarized as per [21]:

$$\hat{\boldsymbol{q}}_t = f(\boldsymbol{q}_{t-1}, \boldsymbol{\omega}_{BI}) = (I_4 + \frac{\Delta t}{2}\boldsymbol{\omega}_{BI})\boldsymbol{q}_{t-1} \tag{12}$$

where $\Delta t$ represents the sensor's sampling time, $\boldsymbol{\omega}_{BI}$ is calculated using Eq. 2, and $\boldsymbol{q}_{t-1}$ denotes the quaternion at the previous sampling time.

The prediction error covariance matrix $\hat{P}$, which characterizes the uncertainty of the state vector prediction, is determined by:

$$\hat{P}_t = F(\boldsymbol{q}_{t-1}, \boldsymbol{\omega}_{BI}) P_{t-1} F(\boldsymbol{q}_{t-1}, \boldsymbol{\omega}_{BI})^T + Q_t \tag{13}$$

Here, $Q_t$ represents the process noise covariance matrix, and the matrix $F$ is calculated as follows:

$$F(\boldsymbol{q}_{t-1}, \boldsymbol{\omega}_{BI}) = \begin{bmatrix} 1 & -\frac{\Delta t}{2}\omega_x & -\frac{\Delta t}{2}\omega_y & -\frac{\Delta t}{2}\omega_z \\ \frac{\Delta t}{2}\omega_x & 1 & \frac{\Delta t}{2}\omega_z & -\frac{\Delta t}{2}\omega_y \\ \frac{\Delta t}{2}\omega_y & -\frac{\Delta t}{2}\omega_z & 1 & \frac{\Delta t}{2}\omega_x \\ \frac{\Delta t}{2}\omega_z & \frac{\Delta t}{2}\omega_y & -\frac{\Delta t}{2}\omega_x & 1 \end{bmatrix} \tag{14}$$

**Correction**

The gyroscope measurements are used to predict the new state of the quaternion. However, there are also sun sensor and magnetometer readings available that can be used to correct the estimation. The corrected state can be computed as follows:

$$q_t = \hat{\boldsymbol{q}}_t + K_t(z_t - h(q_t)) \tag{15}$$

where $z_t = [\boldsymbol{S}_B, \boldsymbol{B}_B]$ is the current sensor measurement, $K_t$ is the Kalman gain and $h_t$ is the observation matrix determined by [21]:

$$h(\hat{\boldsymbol{q}}_t) = \begin{bmatrix} \hat{\boldsymbol{S}}_B \\ \hat{\boldsymbol{B}}_B \end{bmatrix} = 2 \begin{bmatrix} S_{Ix}\left(\frac{1}{2} - q_2^2 - q_3^2\right) + S_{Iy}(q_0q_3 + q_1q_2) + S_{Iz}(q_1q_3 - q_0q_2) \\ S_{Ix}(q_1q_2 - q_0q_3) + S_{Iy}\left(\frac{1}{2} - q_1^2 - q_3^2\right) + S_{Iz}(q_0q_1 + q_2q_3) \\ S_{Ix}(q_0q_2 + q_1q_3) + S_{Iy}(q_2q_3 - q_0q_1) + S_{Iz}\left(\frac{1}{2} - q_1^2 - q_2^2\right) \\ B_{Ix}\left(\frac{1}{2} - q_y^2 - q_z^2\right) + B_{Iy}(q_0q_3 + q_1q_2) + B_{Iz}(q_1q_3 - q_0q_2) \\ B_{Ix}(q_1q_2 - q_0q_3) + B_{Iy}\left(\frac{1}{2} - q_1^2 - q_3^2\right) + B_{Iz}(q_0q_1 + q_2q_3) \\ B_{Ix}(q_0q_2 + q_1q_3) + B_{Iy}(q_2q_3 - q_0q_1) + B_{Iz}\left(\frac{1}{2} - q_1^2 - q_2^2\right) \end{bmatrix} \tag{16}$$

Here, $S_I$ and $B_I$ denote the sun vector and magnetic field in the inertial reference frame, respectively and $R(\boldsymbol{q})$ is the rotation matrix from inertia to body frame.

Due to the nonlinear nature of the measurement equations, it is essential to compute their Jacobian matrix accordingly as:

$$H(\hat{\boldsymbol{q}}_t) = \frac{\partial h(\hat{\boldsymbol{q}}_t)}{\partial q} = 2\begin{bmatrix} \boldsymbol{u}_{SI} & [u_S + \hat{q}_0 \boldsymbol{S}_I]_\times + (\hat{\boldsymbol{q}}_v \cdot \boldsymbol{S}_I) I_3 - \boldsymbol{S}_I \hat{\boldsymbol{q}}_v^T \\ \boldsymbol{u}_{BI} & [\boldsymbol{u}_{BI} + \hat{q}_0 \boldsymbol{B}_I]_\times + (\hat{\boldsymbol{q}}_v \cdot \boldsymbol{B}_I) I_3 - \boldsymbol{B}_I \hat{\boldsymbol{q}}_v^T \end{bmatrix} \tag{17}$$

$$\boldsymbol{u}_{SI} = \boldsymbol{S}_I \times \hat{\boldsymbol{q}}_v \tag{18}$$

$$\boldsymbol{u}_{BI} = \boldsymbol{B}_I \times \hat{\boldsymbol{q}}_v \tag{19}$$

where $q_v = [q_1, q_2, q_3]$ and the remaining elements of the EKF in the correction step are obtained as:

$$S_t = H(\hat{\boldsymbol{q}}_t)\hat{P}_t H^T(\hat{\boldsymbol{q}}_t) + R \tag{20}$$

$$K_t = \hat{P}_t H(\hat{\boldsymbol{q}}_t)\hat{S}_t^{-1} \tag{21}$$

$$P_t = (I_4 - K_t H(\hat{\boldsymbol{q}}_t))\hat{P}_t \tag{22}$$

where $R$ is the measurement noise covariance matrix and $P$ is the covariance matrix.

### 4.2 Control algorithms

#### 4.2.1 Detumbling Mode

Satellites undergo uncontrolled tumbling in space immediately after separation from their launcher, requiring a reduction in angular velocity before normal operations can proceed. Therefore, the primary objective of the ADCS is detumbling, aimed at stabilizing the satellite's motion.

Currently, three different detumbling control algorithms have been evaluated for ST3LLARsat1 considering different sensor configurations and needs. Next, they will be briefly explained and later in Section 5.2 they will be compared and analyzed using MIL simulations.

A key consideration for the development of a detumbling control law is ensuring to produce command proportional to $-\omega$. If both a gyroscope for measuring angular rate and a magnetometer are available during detumbling mode according to satellite design, the approach involving the command of magnetic dipole moments is outlined as follows: [1, 22].

$$\boldsymbol{m} = \frac{k}{\|\boldsymbol{B}_B\|}\boldsymbol{\omega_{BI}} \times \boldsymbol{B}_B \tag{23}$$

where $\boldsymbol{m}$ is a vector with components corresponding to the magnetic moment command aligned with each of the principal axes for magnetorquers and $k$ is the positive control gain.

In case that the magnetometer is the only sensor employed and there is no direct measurement of the angular velocity, the standard b-dot algorithm is given by [1]:

$$\boldsymbol{m} = -\frac{k}{\|\boldsymbol{B}_B\|}\dot{\boldsymbol{B}}_B \tag{24}$$

$$\dot{\boldsymbol{B}}_B = A\dot{\boldsymbol{B}}_O - \boldsymbol{\omega_{BI}} \times \boldsymbol{B}_B \tag{25}$$

Here, $A$ represents the rotation matrix and $\boldsymbol{B}_O$ denotes the magnetic field in the orbital frame. Assuming that for the initial stages of detumbling, $\boldsymbol{B}_O \ll \boldsymbol{B}_B$, Eq. 24 serves as a suitable approximation of Eq. 23.

To accelerate the decay of the spacecraft's spin rate, it is also feasible to use a bang-bang solution of the following form:

$$\boldsymbol{m} = -m_{max}\ sign(\dot{\boldsymbol{B}}_B) \tag{26}$$

where $m_{max}$ represents the maximum torquer dipole. The bang-bang approach operates based on the sign of the magnetic field rate, consistently applying the maximum dipole, which results in increased power consumption.

#### 4.2.2 Pointing Mode

Once the angular velocity of the spacecraft is lower than a given threshold, the satellite switches from detumbling to attitude pointing mode. The main pointing is to nadir, where the aim is to point the -z face of the CubeSat towards Earth in order to communicate and perform the scientific mission. Due to the need of ensuring control performance in the presence of disturbance and uncertainties, a nonlinear controller based on sliding mode control is currently proposed for ST3LLARsat1.

The design algorithm is divided into two main steps: the sliding manifold design and the sliding condition design. To achieve stable satellite motion, a control law is required to force the satellite motion towards the manifold. The sliding condition ensures that the distance from the state to the sliding manifold continuously decreases, and thus, every solution originated outside the sliding manifold converges towards it. The sliding variable $s$ is defined by [23]:

$$\boldsymbol{s} = \boldsymbol{\omega}_{BO} + K_q \boldsymbol{q} \tag{27}$$

where $\boldsymbol{\omega}_{BO}$ is the angular velocity respect to the orbital frame, $\boldsymbol{q}$ is quaternion vector parameters $(q_1, q_2, q_3)$ and $K_q = k_q \; diag(3,3)$ is the sliding manifold design parameter matrix where $k_q$ is a positive constant.

The satellite motion can be described in the space of the sliding variable $\boldsymbol{s}$. The sliding manifold is the subspace of the state space, where the sliding variable equals zero. An equivalent torque $\boldsymbol{T}_{eq}$ is a control torque necessary to keep the satellite on the sliding manifold [23]:

$$\boldsymbol{T}_{eq} = \boldsymbol{\omega}_{BI} \times I\boldsymbol{\omega}_{BI} - \frac{1}{2} I K_q (\boldsymbol{\omega}_{BO} q_0 + \boldsymbol{\omega}_{BO} \times \boldsymbol{q}) - 3\omega_O^2 (\boldsymbol{k}_O \times I\boldsymbol{k}_O) + \omega_O I (\boldsymbol{i}_O \times \boldsymbol{\omega}_{BO}) \tag{28}$$

where $\omega_O$ represents the angular velocity of the satellite around the Earth, determined by the equation $\omega_O^2 = \frac{\mu}{\mathbf{r}^3}$, and $i_O$ and $k_O$ are the unit vector on the orbital frame.

If the satellite is not situated on the sliding manifold, the desired control torque is the sum of the equivalent torque and a component aimed at facilitating the convergence of the sliding variable to zero within a finite time frame [10, 23].

$$\boldsymbol{T}_{des} = \boldsymbol{T}_{eq} - K_s \boldsymbol{s} \tag{29}$$

$$\boldsymbol{m} = \frac{\boldsymbol{B}_B \times \boldsymbol{T}_{des}}{||\boldsymbol{B}_B||^2} \tag{30}$$

Here, the parameter matrix $K_s$ is defined as $K_s = k_s$ diag$(3,3)$, where $k_q$ is a positive constant.

## 5 RESULTS

### 5.1 Simulation Setup

To simulate and validate the developed attitude determination and control algorithms, a model-in-the-loop (MIL) simulator implemented in Matlab/Simulink was used, see Fig. 3.

The simulator comprises four main modules: (i) the environment simulation uses a satellite orbit propagator to generate position and velocity. An International Geomagnetic Reference Field (IGRF) model estimates the magnetic field. Additionally, rotational matrices from inertia to orbital coordinate and body frame are included, along with models for disturbance torques such as aerodynamic drag, solar radiation pressure, gravity gradient, and residual dipole moment; (ii) the dynamic and kinematic module provides the satellite's attitude and angular velocity, influencing both control and disturbance torques; (iii) the sensor and actuator suite discussed in Section 3 is modelled in the sensors and actuators module based on the technical specifications of each equipment; and (iv) the navigation and control module encompasses all algorithms intended for implementation on the ADCS microcontroller. The main parameters considered for simulation are provided in Table 3.

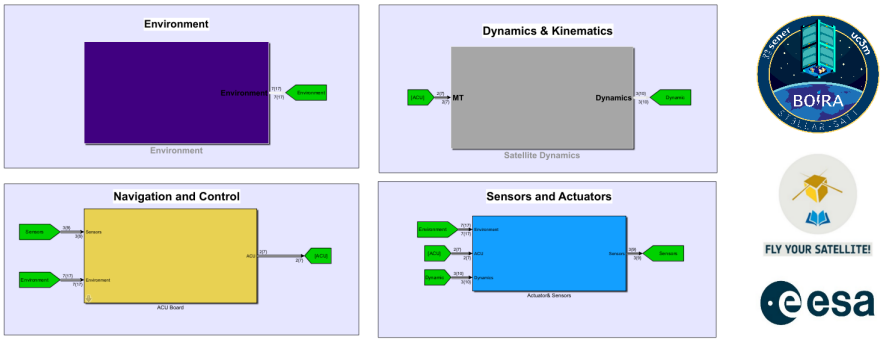


Figure 3: Model-in-the-loop (MIL) architecture for simulating the ADCS subsystem.

Table 3: Mass Properties and Disturbance Parameters Used in MIL simulation.

| Parameter | Symbol | Value | Parameter | Symbol | Value |
|---|---|---|---|---|---|
| MoI (x-axis) | $I_x$ | $0.003\,\mathrm{kg\,m^2}$ | Residual dipole | $m_r$ | $0.001\,\mathrm{A\,m^2}$ |
| MoI (y-axis) | $I_y$ | $0.003\,\mathrm{kg\,m^2}$ | Solar Power | $P_s$ | $1376\,\omega/\mathrm{m^2}$ |
| MoI (z-axis) | $I_z$ | $0.001\,\mathrm{kg\,m^2}$ | Air density | $\rho$ | $3.76 \times 10^{-12}\mathrm{kg/m^3}$ |
| Dimension | $d$ | [0.1,0.1,0.2] cm | CoP and CoM offset | $L_{mp}$ | 1 cm |
| Mass | $m$ | 1.05 kg | Drag Coefficient | $C_d$ | 2 |

†MoI, COP and CoM denotes Moment of Inertia, Center of Pressure and Center of Mass respectively.

† $\rho$ denotes the density under high solar activity.

### 5.2 Detumbling

As outlined in Section 4.2.1, three detumbling control algorithms are currently considered for ST3LLARsat1. This section aims to analyze and compare them for a mission scenario using the worst initial condition of $\omega = [90, 90, 90]\ \mathrm{deg/s}$ with absolute amount of $||\omega|| = 155.8\,\mathrm{deg/s}$. It is noted that the aim is to reach the desired amount of $||\omega_{th}|| = 1\,\mathrm{deg/s}$, which serves as the threshold value for transitioning to nadir pointing mode.

The results are presented in Fig. 4. The left plot shows the time-domain comparison of the three detumbling control approaches whereas the right plot their average power consumption.

The bang-bang controller (see blue line in Fig. 4 – left plot) is able to reduce the angular velocity, but there exists a minimum rate that it cannot surpass. In contrast, all other two methods can effectively reduce angular velocity to the desired threshold, $\boldsymbol{\omega}_{th}$. Specifically, for the $\boldsymbol{\omega} \times \boldsymbol{B}$ and b-dot methods, this threshold is achieved at orbital times of 2.12 and 2.25, respectively. This comparison shows that despite the fact that the $\boldsymbol{\omega} \times \boldsymbol{B}$ algorithm utilizes both gyroscope and magnetometer data, the deorbiting time is not significantly lower compared to the b-dot algorithm, which relies solely on magnetometer data.

Furthermore, the comparison of average power consumption (Fig. 4 – right plot) indicates that the bang-bang algorithm consumes more power (1.08 $W/T$) than the b-dot and $\boldsymbol{\omega} \times \boldsymbol{B}$ algorithms (0.2 $W/T$ and 0.64 $W/T$ respectively). Additionally, the $\boldsymbol{\omega} \times \boldsymbol{B}$ algorithm, which incorporates gyroscopes as well as magnetometers, consumes more power compared to b-dot algorithms. Both b-dot and $\boldsymbol{\omega} \times \boldsymbol{B}$ algorithms employ proportional gains, meaning they apply torque according to the angular velocity of the body, as opposed to bang-bang algorithms, which apply the maximum amount of torque based on the sign of rotation.

Based on the above power consumption and deorbit time analysis, and considering the slight difference in deorbit time between the b-dot and $\boldsymbol{\omega} \times \boldsymbol{B}$ algorithms, along with the considerable

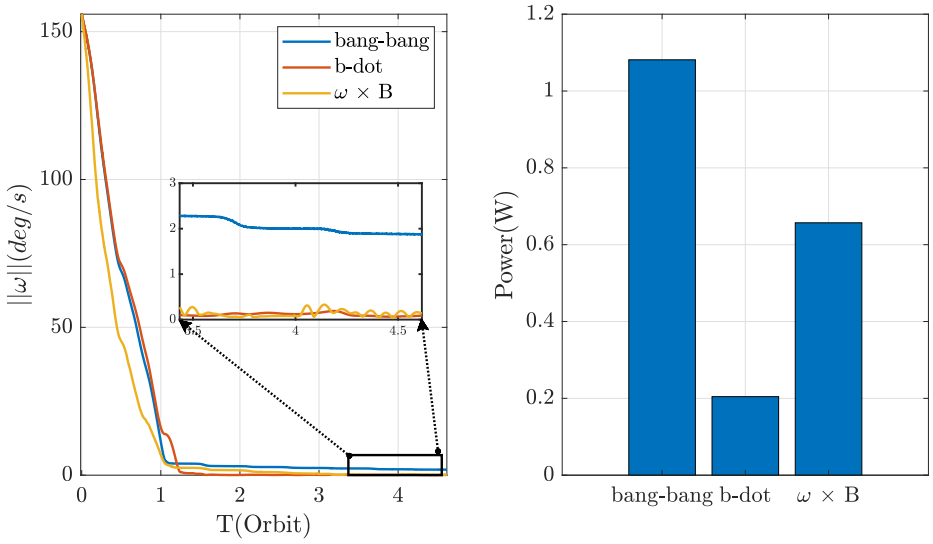


Figure 4: Comparison of changes in absolute angular velocities during the detumbling mode.

difference in power consumption, the b-dot algorithm appears to be the most effective choice for detumbling mode for the tested scenario. It is noted that a different strategy could be used depending on the value of the angular rates, such as: use the bang-bang controller when $\boldsymbol{\omega}$ is very high, then switch to the $\boldsymbol{\omega} \times \boldsymbol{B}$ controller to quickly reduce the rotation down to a TBD $||\omega_{th}||$, for example from 90 to 25 degrees/seconds, and then fine-tune and nominally operate with the b-dot controller.

Fig. 5 shows the time history of angular rate in three axes using the b-dot algorithm, considering a worst-case initial value of $\boldsymbol{\omega} = [90, 90, 90]$ deg/s. During this simulation, a duty cycle of 80% for applying torque and 20% for reading the magnetic field by the magnetometer is considered to remove the interaction of the magnetic torque on the measurement.

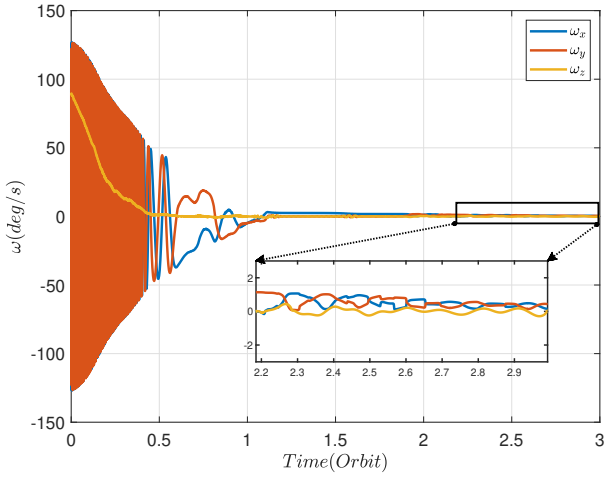


Figure 5: Change of angular velocity using b-dot algorithm

### 5.3 Attitude Pointing - nadir case

According to the defined mission scenario, once the satellite reaches an angular velocity of $\boldsymbol{\omega}_{th}$, it enters the nadir pointing phase. Fig. 6 (upper plot) shows the pointing errors in the time domain starting right after the nadir pointing mode is activated.

The SMC controller achieves nadir pointing with the required accuracy of APE $\leq 10\,\mathrm{deg}$ in approximately 8 orbital periods after entry into the nadir pointing phase. By the 14th orbital period, the pointing accuracy is further improved to within $5\,\mathrm{deg}$. Throughout these simulations, all disturbance torques were accounted for, and the controller, in the presence of these disturbances, successfully maintains the required pointing accuracy. The gains assigned to the SMC controller for $K_s$ and $K_q$ are $9 \times 10^{-8}$ and $5.5 \times 10^{-4}$, respectively.

During this phase, the EKF serves as the primary attitude determination algorithm, initialized with a previous estimate obtained from the Triad method. Fig. 6 (bottom plot) shows the EKF error in the presence of eclipses (highlighted areas represent the illumination period). It is observed that the accuracy of the EKF for all attitude angles remains better than $3\,\mathrm{deg}$. The algorithm primarily uses the magnetometer as the main sensor for the correction step due to its superior accuracy compared to photodiodes. Consequently, the attitude determination error does not increase during eclipse periods.

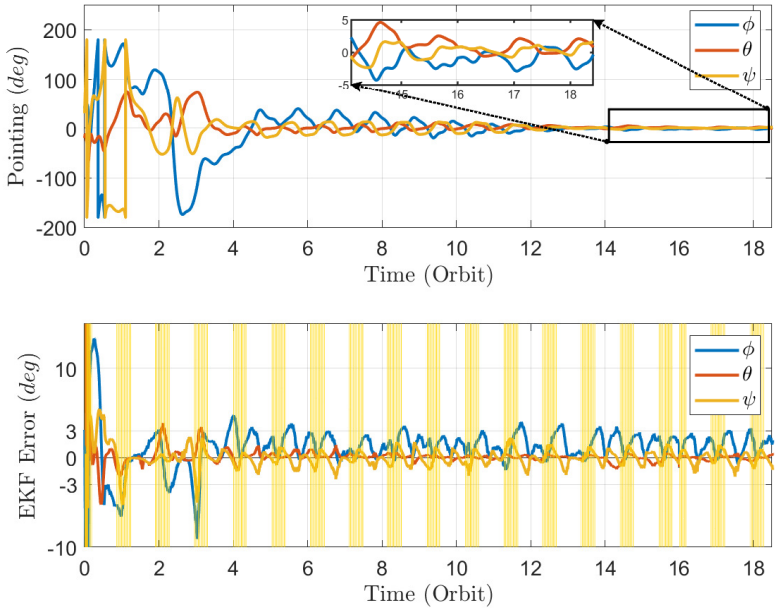


Figure 6: Pointing accuracy (top) & attitude estimation error (bottom) during nadir pointing phase

### 5.4 Monte Carlo (Uncertainty) analysis

To evaluate the performance of the algorithms, an uncertainty analysis using Monte Carlo simulation was conducted. This analysis encompasses both operational modes of detumbling and nadir pointing, taking into account the range of uncertainty parameters provided in Table 4.

Table 4: Uncertainty range of the parameters considered in the analysis.

| Variable | Uncertainty | Operational Mode |
|---|---|---|
| Moment of inertia | $\pm 10\%$ | Detumbling- Pointing |
| CoM and CoP offset | $\pm 10\%$ | Detumbling- Pointing |
| Air density | $\pm 10\%$ | Detumbling- Pointing |
| Initial angular velocity | $\pm[90, 90, 90]\mathrm{deg/s}$ | Detumbling |
| Initial attitude | $\pm[0, 2\pi]$ | Pointing |
| Initial angular velocity | $\pm[0, 1]\mathrm{deg/s}$ | Pointing |

As reported in the SwissCube mission report [24], the satellite's rate after release was approximately $90\,\mathrm{deg/s}$ around the y-axis. Therefore, to assess the detumbling algorithm's performance under worst-case conditions, the magnitude of the initial angular velocity in Monte Carlo analysis was held constant at $||\boldsymbol{\omega}|| = \sqrt{90^2 + 90^2 + 90^2} \approx 155\,\mathrm{deg/s}$, while the vector components were generated randomly accordingly. Additionally, regarding air density, the average value was considered under worst-case conditions of high solar activity predicted for summer 2025. However, a 10% error was also considered for inaccuracies in the predicted value.

The Monte Carlo analysis for the detumbling mode is presented in Fig. 7. The results show that the b-dot algorithm is able to reduce $\boldsymbol{\omega}$ to $\boldsymbol{\omega}_{th}$ under the considered uncertainty. The implementation of the b-dot algorithm involves taking measurements twice per second. Considering the frequency of ADCS operation is $10\,\mathrm{Hz}$, Monte Carlo analysis demonstrates that even at high angular rates leading to rapid changes in the magnetic field, this approach of reading sensor measurements when magnetic torquers are switched off maintains its performance. The simulation results also show that the absolute value of the angular rate for the entire uncertain conditions reaches $\boldsymbol{\omega}_{th}$ within less than 6 orbital periods.

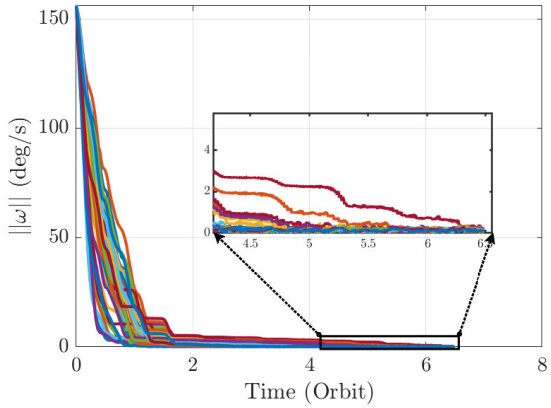


Figure 7: Monte Carlo simulation for the detumbling mode

The Monte Carlo simulation for the nadir pointing mode is presented in Figure 8. The results show the ability of the SMC controller to maintain an attitude pointing error (APE) lower than $10\,\mathrm{deg}$, considering different uncertainties and disturbances applied to the satellite as described in Table 4. In all the simulations, the desired pointing was achieved after 10 orbital periods.

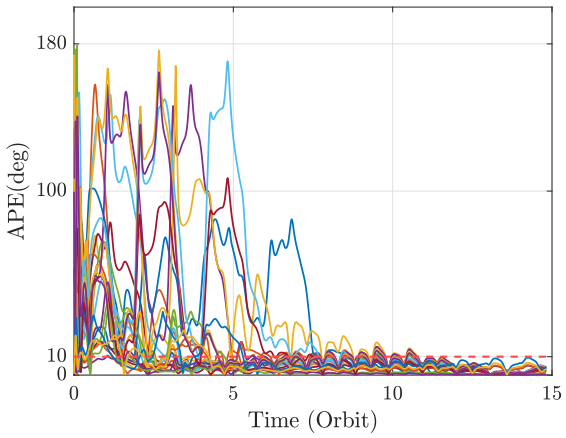


Figure 8: Monte Carlo simulation for the nadir pointing mode

## 6 CONCLUSIONS

This paper presents the ADCS design for the ST3LLARsat1 mission. The attitude control system for the different ADCS operational modes, including detumbling and nadir pointing, relies on pure magnetic actuation. By employing b-dot algorithms, which exhibit superior effectiveness in terms of power consumption and deorbit time, the angular velocity can be reduced from a worst-case scenario of $90\,\mathrm{deg/s}$ for each axis to $1\,\mathrm{deg/s}$ within a 2.25 orbital time. Additionally, the sliding mode controller for nadir pointing achieves pointing errors lower than $5\,\mathrm{deg}$. Using photodiodes, magnetometers, and gyroscopes as commercial-off-the-shelf (COTS) sensors and implementing a hybrid approach combining the Triad and Extended Kalman Filter (EKF) algorithm result in attitude estimation accuracy lower than $3\,\mathrm{deg}$. A Monte Carlo campaign with uncertainties in mass properties, initial attitude, and rate values, validate the algorithms' performance in these conditions.


## ACKNOWLEDGMENT

ST3LLARsat1 is funded by the UC3M-SENER Aerospace academic-industry chair ST3LLAR, the Aerospace department at UC3M, and two following prof. Andrés Marcos's awards: (1) the Beatriz Galindo Distinguished Senior Investigator by the Spanish Government, and (2) the Madrid Government ("Comunidad de Madrid") under the Multiannual Agreement with UC3M in the line of "Research Funds for Beatriz Galindo Fellowships" (SPACEROBCON-CMUC3M) within the V PRICIT (Regional Programme of Research and Technological Innovation).

The authors also gladly acknowledge the support of the Education Office of the European Space Agency under the pilot educational Fly Your Satellite! Design Booster Programme. The contents and ideas in this article are the sole responsibility of its authors.


## REFERENCES


[1] F. L. Markley and J. L. Crassidis, *Matrices, Vectors, Frames, Transforms*. New York, NY: Springer New York, 2014, pp. 17–65. [Online]. Available: https://doi.org/10.1007/978-1-4939-0802-8_2

[2] J.-J. Slotine and W. Li, *Applied Nonlinear Control*. Englewood Cliffs: Prentice Hall, 1991.

[3] T. A. W. Dwyer and H. Sira-Ramirez, "Variable-structure control of spacecraft attitude maneuvers," *Journal of Guidance, Control, and Dynamics*, vol. 11, no. 3, pp. 262–270, 1988.

[4] M. Psiaki, "Magnetic torquer attitude control via asymptotic periodic linear quadratic regulation," *IEEE Transactions on Aerospace and Electronic Systems*, vol. 37, no. 1, pp. 143–153, 2001.

[5] M. Lovera, E. De Marchi, and S. Bittanti, "Periodic attitude control techniques for small satellites with magnetic actuators," *IEEE Transactions on Control Systems Technology*, vol. 10, no. 1, pp. 90–95, 2002.

[6] R. Wiśniewski and M. Blanke, "Fully magnetic attitude control for spacecraft subject to gravity gradient," *Automatica*, vol. 35, no. 7, pp. 1201–1214, 1999. [Online]. Available: https://www.sciencedirect.com/science/article/pii/S0005109899000217

[7] F. Celani, "Robust three-axis attitude stabilization for inertial pointing spacecraft using magnetorquers," *Acta Astronautica*, vol. 107, pp. 87–96, 2015. [Online]. Available: https://www.sciencedirect.com/science/article/pii/S0094576514004615

[8] R. Wisniewski, *Satellite Attitude Control Using Only Electromagnetic Actuation*. Aalborg Universitetsforlag, 1997.

[9] M. Ovchinnikov, D. Roldugin, V. Penkov, S. Tkachev, and Y. Mashtakov, "Fully magnetic sliding mode control for acquiring three-axis attitude," *Acta Astronautica*, vol. 121, pp. 59–62, 2016. [Online]. Available: https://www.sciencedirect.com/science/article/pii/S009457651530120X

[10] A. Sofyali and E. Jafarov, "Purely magnetic spacecraft attitude control by using classical and modified sliding mode algorithms," in *Proceedings of the 12th International Workshop on Variable Structure Systems*, Mumbai, 2012, pp. 117–123.

[11] H. D. Black, "A passive system for determining the attitude of a satellite," *AIAA J.*, vol. 2, pp. 1350–1351, 1964.

[12] M. D. Shuster and S. D. O'Hanlon, "Three-axis attitude determination from vector observations," *Journal of Guidance, Control, and Dynamics*, vol. 4, no. 1, 1981.

[13] R. E. Kalman, "A new approach to linear filtering and prediction problems," *Journal of Basic Engineering*, vol. 82, pp. 35–45, 1960.

[14] Y. Yang, "Spacecraft attitude determination and control: Quaternion based method," *Annual Reviews in Control*, vol. 36, no. 2, pp. 198–219, 2012.

[15] Xsens Technologies B.V., *MTi and MTx User Manual and Technical Documentation*, Xsens Technologies B.V., Pantheon 6a, 7521 PR Enschede, The Netherlands, May 2009.

[16] MicroStrain Inc., *3DM-GX3-25 Miniature Attitude Heading Reference Sensor*, 1st ed., 459 Hurricane Lane, Suite 102, Williston, VT 05495, USA, 2009.

[17] VectorNav Technologies, LLC, *VN-100 User Manual*, preliminary ed., College Station, TX 77840, USA, 2009.

[18] InterSense, Inc., *InertiaCube2+ Manual*, 1st ed., 36 Crosby Drive, Suite 150, Bedford, MA 01730, USA, 2008.

[19] J. R. Wertz, *Spacecraft Attitude Determination and Control*. Kluwer Academic, 1978.

[20] W. J. L. J.R. Wertz, *Space Mission Analysis and Design*. Springer Dordrecht, 1999.

[21] A. M. Sabatini, "Kalman-filter-based orientation determination using inertial/magnetic sensors: Observability analysis and performance evaluation," *Sensors*, vol. 11, no. 10, pp. 9182–9206, 2011. [Online]. Available: https://www.mdpi.com/1424-8220/11/10/9182

[22] G. Avanzini and F. Giulietti, "Magnetic detumbling of a rigid spacecraft," *Journal of Guidance, Control, and Dynamics*, vol. 35, pp. 1326–1334, 07 2012.

[23] D. Ivanov, M. Kushniruk, and M. Ovchinnikov, "Study of satellite formation flying control using differential lift and drag," *Acta Astronautica*, vol. 152, pp. 88–100, 2018. [Online]. Available: https://www.sciencedirect.com/science/article/pii/S009457651830540X

[24] E. Portal. Swisscube satellite missions. Accessed: April 4, 2024. [Online]. Available: https://www.eoportal.org/satellite-missions/swisscube